


Local Spin Seebeck Imaging with a Scanning Thermal Probe

Alessandro Sola^{1,*}, Craig Barton², Vittorio Basso¹, Carsten Dubs³, Massimo Pasquale¹ and Olga Kazakova²

¹*Istituto Nazionale di Ricerca Metrologica, Strada delle Cacce 91, 10135 Turin, Italy*

²*National Physical Laboratory, Teddington TW11 0LW, United Kingdom*

³*INNOVENT e.V., Technologieentwicklung, Prüssingstraße 27B, 07745 Jena, Germany*

 (Received 19 May 2020; revised 17 August 2020; accepted 26 August 2020; published 22 September 2020)

We present the results of an experiment to locally resolve the spin Seebeck effect in a high-quality yttrium iron garnet–Pt sample. We achieve this by using a locally heated scanning thermal probe to generate a highly local nonequilibrium spin current. To support our experimental results, we also present a model based on the nonequilibrium thermodynamic approach that is in a good agreement with the experimental findings. To further corroborate our results, we index the locally resolved spin Seebeck effect with that of the local magnetization texture by magnetic force microscopy and correlate corresponding regions. We hypothesize that this technique allows imaging of magnetization textures within the magnon diffusion length and hence characterization of spin-caloritronic materials at the nanoscale.

DOI: [10.1103/PhysRevApplied.14.034056](https://doi.org/10.1103/PhysRevApplied.14.034056)

I. INTRODUCTION

The visualization of domain structure in magnetism and magnetic materials is paramount in aiding the understanding at the fundamental level and subsequent use of such materials in real-world applications. Hence, a significant effort is dedicated to the development of a variety of techniques that are suitable for studying magnetic materials and magnetic domains. Magnetic force microscopy (MFM) [1,2] is a scanning-probe technique capable of sensing the force gradients induced by stray fields over the surface of a magnetic material at the nanoscale. Scanning electron microscopy with polarization analysis [3] can also be used to visualize magnetic domains by monitoring the spin polarization of the secondary electrons interacting with the stray field of a sample under test. To visualize the local magnetization $M(r)$ [or the flux density $B(r)$] instead of the stray field $H(r)$, it is possible to use imaging techniques such as magneto-optic effects [4] or Lorentz microscopy [5]. Electrons can also be used as a probe for the imaging of magnetic domains in electron holography [6]. The aforementioned techniques typically involve the characterization of magnetic properties confined to the surface or thin samples; the investigation of the domain structure in bulk materials, however, requires more-complex experiments that involve neutron scattering [7–10] or x-ray spectroscopy [11–13].

The interaction between heat and nonequilibrium spin currents in magnetic materials is an alternative approach

for imaging magnetic domains. Analogous to standard thermoelectric effects, this interaction has been described as the thermal generation of driving power for electron spin; that is, the spin Seebeck effect (SSE) [14]. This effect involves pure spin currents that are produced by driving the system out of equilibrium through thermal gradients; by definition, they carry zero net charge and depend on the local magnetization of the material. The length scale l_M that governs the SSE has been demonstrated to be on the order of micrometers [15–17]. The SSE has been observed in magnetic insulator garnet ferrites [18] such as the ferrimagnetic yttrium iron garnet ($Y_3Fe_5O_{12}$; YIG), or other ferrites [19–21]. A typical spin Seebeck device can be formed by creating a bilayer of a magnetic material and a thin metallic film with high spin-orbit coupling such as platinum or tungsten, both of which are paramagnetic heavy metals. This second layer acts as the spin detector because of the inverse spin Hall effect that enables a spin-charge conversion at the interface [22]. The most-useful configuration is the longitudinal spin Seebeck effect [23–25], which corresponds to the generation of a spin current parallel to the temperature gradient, both of which are orthogonal to the local magnetization direction, which is in the sample plane. Most experiments typically involve spin Seebeck samples that are uniformly heated over the whole surface and are in a uniform magnetic state (i.e. at or near saturation). In these conditions, it is possible to compare the spin Seebeck characteristics with the magnetization loop of the sample; however, it is not possible to resolve the contributions to the spin Seebeck signal coming from regions where the orientation of the magnetization

*a.sola@inrim.it

differs from the average (i.e., in a multidomain state). To resolve magnetic domains, it is necessary to go beyond the experimental configuration previously described in favor of a locally injected heat current, as described in Fig. 1. The dependence of a local spin Seebeck signal on the local magnetization has been observed by scanning a laser beam on a YIG/Pt structure [26] and in a time-resolved configuration [27–29]. By taking account of the experimental geometry, one can use the same setup for the measurement of the time-resolved anomalous Nernst effect [26,30]. In this work we present local measurements of the SSE using a scanning thermal probe as local source of heat and nonequilibrium spin currents. We use a high-quality bulk YIG single crystal with a Pt strip lithographically defined on the surface as our spin detector. The thickness of the YIG single crystal is selected so that it is much greater than any magnon diffusion length l_M reported for YIG. This configuration allows us to approximate the sample as a semi-infinite geometry in which we can assume spherically symmetric heat propagation and its contribution to the spin Seebeck signal according to the magnon diffusion length. We demonstrate that the measured effect is unambiguously the local spin Seebeck effect through a series of tests by our varying the heating power and the vector of the externally applied magnetic field. We interpret and support our observations with a thermodynamic description of the generation of the local magnetic moment current. This model describes quantitatively the geometry of local heat current as a circular heat source below the thermal probe, whose size is larger than the cross section of the tip due to the nonzero thermal conductivity at the YIG/Pt interface. The diameter of the heat source that we observe by using our model is approximately $2.8 \mu\text{m}$.

II. SPIN SEEBECK EFFECT BY UNIFORM AND LOCAL HEATING

Two variations of a spin Seebeck experiment are shown in Fig. 1, both demonstrating that the measured signal due to the inverse spin Hall effect (represented by the yellow wires in Fig. 1) corresponds to the open-circuit voltage across the Pt film. Since there are no electric currents flowing in an open-circuit configuration, we can exclude any magnetoresistance contributions to the signal, such as the spin Hall magnetoresistance that is usually observed in bilayers formed by a magnetic material and a heavy metal. The first configuration [Fig. 1(a)] represents the “classic” experimental geometry reported for the majority of experimental results. This provides a uniform distribution of the thermally generated spin current as a consequence of the heat current across the whole surface of the sample. The proportionality between the voltage gradient $\nabla_y V_{\text{SSE}}$ generated along the Pt film due to the SSE and the heat current I_q passing through the sample along the cross section A is described by the following expression:

$$\frac{\nabla_y V_{\text{SSE}}}{I_q} \kappa A = \theta_{\text{SH}} \left(\frac{\mu_B}{e} \right) \frac{v_{\text{YIG}} l_{\text{YIG}} \epsilon_{\text{YIG}}}{v_p} \frac{1}{t_{\text{Pt}}}, \quad (1)$$

where μ_B/e is the ratio between the Bohr magneton and the elementary charge, and κ is the thermal conductivity of YIG. The other parameters in Eq. (1) are the spin Hall angle θ_{SH} , the absolute thermomagnetic power coefficient ϵ_{YIG} , the magnon diffusion length l_{YIG} , and the thickness of the Pt film t_{Pt} . The intrinsic magnetic moment conductance of YIG is represented by $v_{\text{YIG}} = l_{\text{YIG}}/\tau_{\text{YIG}}$, where τ_{YIG} is the magnon mean scattering time. The parameter v_p

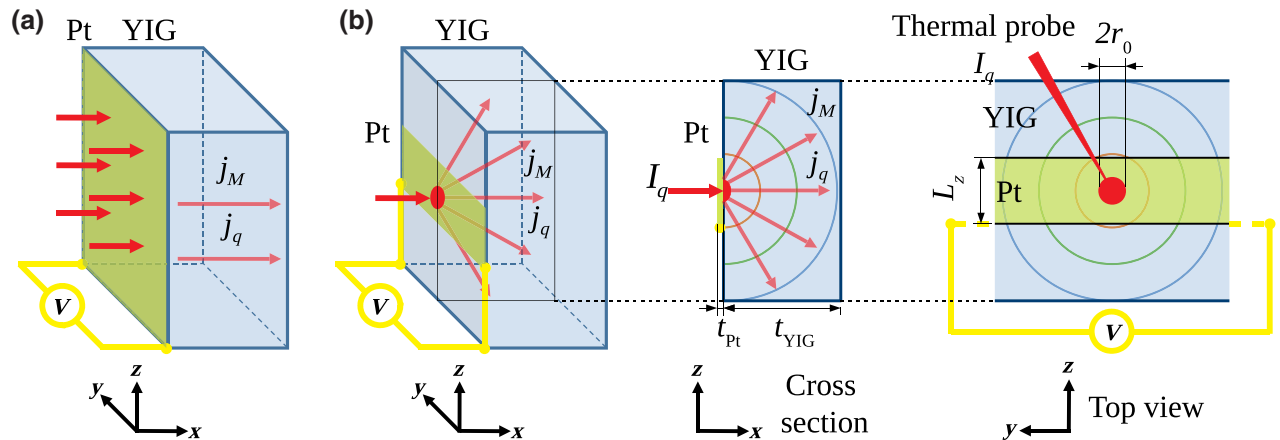


FIG. 1. Longitudinal spin Seebeck measurement configurations. (a) Standard configuration with uniform heating (the red arrows at the YIG/Pt interface represent the hot side; the cold side is at the right-hand side of the YIG slab). (b) Local heating from the Pt side generates a magnetic moment current density j_M in spherical symmetry. The projections of the experimental scheme on the x - z and y - z planes are presented on the right side of the panel: the local heat current i_q from the thermal probe spreads over a circle whose dimensions (r_0) limit the spatial resolution. For the YIG/Pt sample that we investigate, the dimensions are $t_{\text{Pt}} = 5 \text{ nm}$, $t_{\text{YIG}} = 0.5 \text{ mm}$, and $L_z^{\text{Pt}} = 150 \mu\text{m}$.

represents the magnetic moment conductance per unit surface area of the YIG/Pt bilayer. This quantity depends on the intrinsic conductances of YIG and Pt, and on the ratio between the thickness and the magnon diffusion length for each layer. We derive the expression for v_p from a thermodynamic description of the generation of magnetic moment currents [31]. It is important to note that the geometry shown in Fig. 1 and modeled by Eq. (1) does not allow us to resolve the spatial distribution of the underlying magnetic structure, since the spin Seebeck voltage results from an averaged contribution of regions with different magnetization. Because of this, the experiments performed in this geometry are usually conducted at magnetic saturation or follow the magnetization hysteresis loop.

In the second experimental setup [Fig. 1(b)], which shows the effect of the heated probe in contact with the Pt surface, we can selectively generate the heat current injected through a point of the Pt surface and propagating with spherical symmetry in the volume. In this arrangement, the thermally generated spin current is assigned to a locally limited SSE, which is generated at the point of thermal contact, represented by the red dot in Fig. 1(b). As in the standard configuration, the spin Seebeck voltage depends on the average magnetization, and in the configuration with local heating the effect scales with the magnetization of a region whose size is determined by the locally heated volume, allowing resolved measurements of the domain distribution within the sample. To describe this experimental configuration, we take into account the local magnetization $\hat{\mathbf{m}}$ as a unit vector. This leads to an expression for the spin Seebeck voltage, originating from a circle with radius r_0 on the top of the sample, into which a heat current I_q is injected. In this way it is possible to rewrite Eq. (1) as follows:

$$\frac{\nabla_y V_{\text{SSE}}}{I_q} 2\pi r_0^2 k = \theta_{\text{SH}} \left(\frac{\mu_B}{e} \right) \frac{v_{\text{YIG}} l_{\text{YIG}} \epsilon_{\text{YIG}}}{v_p} \frac{1}{t_{\text{Pt}}}, \quad (2)$$

where the dependence on the radius of the heated region r_0 [red circle in Fig. 1(b)] is highlighted. However, the value of V_{SSE} in Eq. (2), and in particular the voltage difference ΔV_{SSE} , is the one that would be measured at the two ends of the heated region, limited by r_0 . Since this quantity is not accessible by the experiment, it is necessary to rescale the value of ΔV_{SSE} , taking into account the lateral dimensions of the whole Pt film that works as the spin-voltage detector. Here we use an approximation criterion and consider the Pt film as an electric circuit formed by a voltage source (V_{SSE}), two resistances in series whose sum is proportional to $(L_y - 2r_0)/2r_0$, and one resistance in parallel whose value is proportional to $L_y/(L_z - 2r_0)$. Assuming that $2r_0 \ll L_y$ and $2r_0 \ll L_z$, we can represent the experimental values of the spin Seebeck voltage as a rescaled

value of ΔV_{SSE} :

$$\Delta V_{\text{SSE,exp}} \simeq \Delta V_{\text{SSE}} \frac{2r_0}{L_z}. \quad (3)$$

The expression for $\Delta V_{\text{SSE,exp}}$ can be used to interpret the experimental data of the local SSE. By using the parameters included in Eq. (2) to determine the value of V_{SSE} on the right of Eq. (3), we can obtain a value of r_0 that can be considered as the spatial resolution of the spin Seebeck imaging.

III. EXPERIMENTAL METHODS

The measurements of the local SSE are performed on a high-quality YIG single-crystal plate ($L_y = 4.95$ mm, $L_z = 3.91$ mm, and thickness $t_{\text{YIG}} = 0.545$ mm). Both crystal surfaces are polished to be optically flat [$R_q = 0.4$ nm obtained by atomic force microscopy (AFM)]. A $150\text{-}\mu\text{m}$ -wide Pt strip is sputtered onto one side of the YIG crystal along the y direction, where the z direction defines the strip width. A Pt thickness t_{Pt} of approximately 5 nm is chosen to maximize the V_{SSE} signal. This value is selected on the basis of our model [t_{Pt} dependence in Eqs. (1) and (2)] and the information on the spin diffusion length of Pt, as well as previously published experimental values [32,33]. The measurement technique for the uniform heat current (i.e., the classic configuration) has been described elsewhere [34] for the same sample. The local heat current is generated with a nano-thermal-analysis probe (nanoTA probe); this consists of a micropatterned AFM cantilever probe that allows a current to be driven around the cantilever, resulting in Joule heating that propagates to the tip apex. We approximate the temperature of the probe using a series of polymer test samples with known glass transition temperatures. We also expect an offset in our estimated temperatures due to the respectively higher thermal conductivity of the Pt used in our studies as compared with the test polymers. With this procedure we obtain an approximate relationship between the probe-power voltage and the temperature difference applied to the sample in this geometry. Moreover, we observe a stable spin Seebeck signal when reversing the heating voltage, thus verifying the absence of electric interference from the nanoTA cantilever. This setup allows us to compare a local domain map obtained by MFM with a local SSE map and correlate the two data sets. The enlarged area in Fig. 2(a) represents one of the specific regions investigated in the experiments. From the data in Figs. 2(b) and 2(c) it is possible to spatially map the SSE voltage at the location of the thermal probe in contact with the Pt film. This makes it possible to correlate the SSE and MFM maps and draw qualitative conclusions. Figures 2(b) and 2(c) show a stray field gradient at the YIG surface obtained by MFM [Fig. 2(b)] and a SSE map obtained by nanoTA [Fig. 2(c)]. The experiment

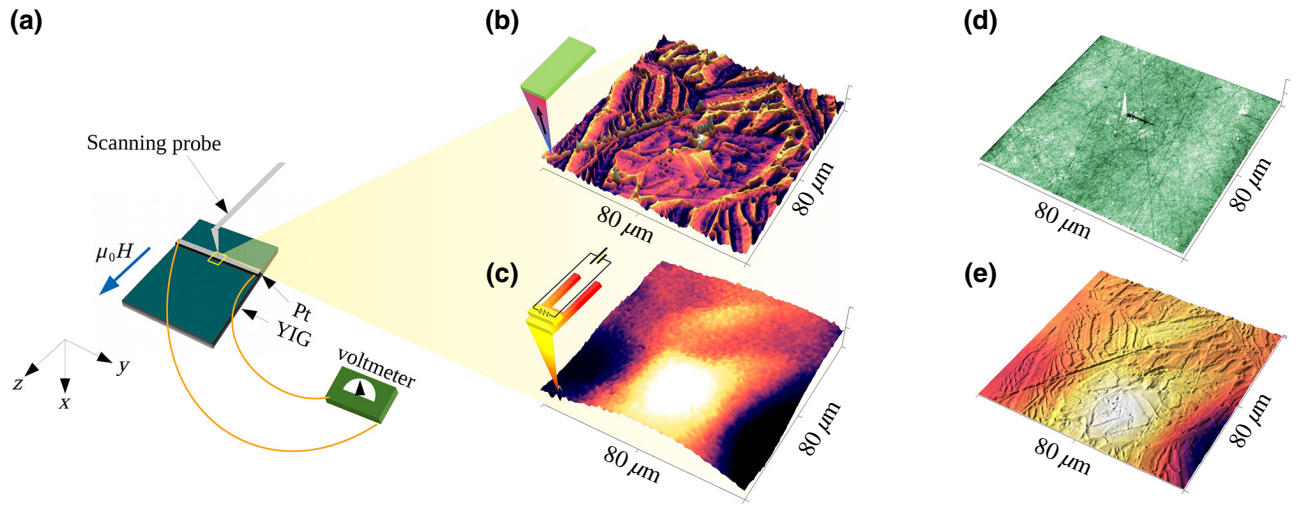


FIG. 2. Experimental setup for the local SSE measurements. (a) Macroscopic schematic representation of the YIG/Pt sample with the nanovoltmeter connected at the edges of the Pt strip. The images in (b)–(e) are examples of measurements obtained from a $80 \times 80 \mu\text{m}^2$ area of the Pt film with an applied magnetic field of approximately 8 mT. (b) MFM image of the same $80 \times 80 \mu\text{m}^2$ area. (c) Spin Seebeck voltage originating from the scanning thermal probe. (d) AFM image obtained both from the MFM map and the local spin Seebeck map. (e) Three-dimensional image obtained by our overlapping the MFM map and the spin Seebeck map, taking into account the information on their mutual shift provided by the AFM images.

is structured as follows: First we perform a set of nanoTA measurements with a saturating magnetic field in both directions ($\pm M_s$), achieved with use of a small neodymium magnet adjacent to the sample. This corresponds to a standard SSE experiment. The second set of measurements is performed at a magnetic field, where a domain structure can be observed by MFM. Keeping the applied field constant, we perform the nanoTA measurements at different heating power levels of the thermal probe and at several points of the sample surface, including the transition from the Pt strip to the bare YIG surface.

IV. RESULTS AND DISCUSSION

A. Local spin Seebeck effect in the saturated state

We first investigate the local SSE of the YIG/Pt bilayer structure at magnetic saturation. This experiment is performed with the field aligned within the plane of the sample and perpendicular to the long axis of the Pt strip [Fig. 2(a)]. The experimental data points in Fig. 3 show the SSE data for each realized temperature difference ΔT .

We average the signal that originates from the local heating of a $40 \times 20 \mu\text{m}^2$ area of the Pt surface, and the experimental uncertainty is evaluated from the standard deviation of these data sets. The dependency of the total measured voltage, including the spin Seebeck contribution, on ΔT can be described by the following relation:

$$V_{\text{meas}} = \pm C_{\text{SSE}} \Delta T + C_{\text{OSE}} \Delta T + V_0, \quad (4)$$

where V_{meas} corresponds to the average voltage recorded as a consequence of scanning a given area and ΔT is

the difference between the probe temperature and room temperature. The voltage V_{meas} contains the following contributions: The first one ($C_{\text{SSE}} \Delta T$) corresponds to the spin Seebeck voltage $V_{\text{SSE,exp}}$ of Eq. (3); the sign of the spin Seebeck coefficient $\pm C_{\text{SSE}}$ depends on the direction of the magnetization. The second contribution is the ordinary Seebeck effect (C_{OSE}); for our work, this is a spurious component that does not depend on the magnetic configuration of the sample. The C_{OSE} component derives from

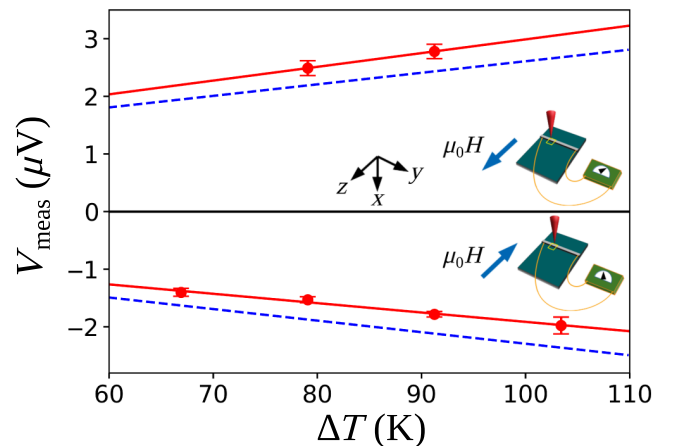


FIG. 3. Measured voltage as consequence of the local heating of the sample at magnetic saturation: spin and ordinary Seebeck voltage as a function of the temperature difference (red points). The dashed blue lines are fitting lines after the compensation of the ordinary Seebeck component. The direction of the saturating magnetic field is shown as a sketch in each panel.

the contact between the different metals used to electrically connect the sample (silver paint for bonding the platinum strip at the edges of the thin film). This is due to a small transverse heat loss through the electric contacts associated with small geometric asymmetry. Such an artifact can affect the interpretation of spin-caloritronic measurements and has been described for both the spin Seebeck effect and the spin Peltier effect [34] data. The last contribution in Eq. (4) is an offset voltage V_0 that originates from the circuit resistance. The voltage due to the Seebeck effects, both spin and ordinary effects, can be plotted as a function of ΔT , according to Eq. (4). From the difference between the absolute values of the slopes obtained from the linear fits shown in Fig. 3 (red lines), a clear distinction can be made between the ordinary Seebeck component and the spin Seebeck component. After the compensation of the ordinary Seebeck component, we present the spin Seebeck data as dashed blue lines in Fig. 3, whose coefficient is $C_{\text{SSE}} = 2 \times 10^{-8} \text{ V K}^{-1}$.

B. Local spin Seebeck effect in the multidomain state

In the second step, we repeat the measurements with a lower applied magnetic field to induce a reduction in the magnetostatic energy of the sample and introduce a domain structure where we can distinguish several magnetization areas from the MFM images. We apply the magnetic field at a lower level by distancing the neodymium magnet from the sample and we measure its value by positioning a Hall probe in place of the sample. The measured value of the applied magnetic field is approximately 8 mT. An example of two MFM images of the sample at magnetic saturation and with an applied field of approximately 8 mT obtained from the same area is presented in Fig. 4. Having applied approximately 8 mT, we scan the thermal probe over a $80 \times 80 \mu\text{m}^2$ surface in the same locations as for the MFM at different values of ΔT to analyze the voltage that arises from the local SSE. We use five values of the heating power on the thermal probe, which lead to the corresponding temperature differences ΔT at each area

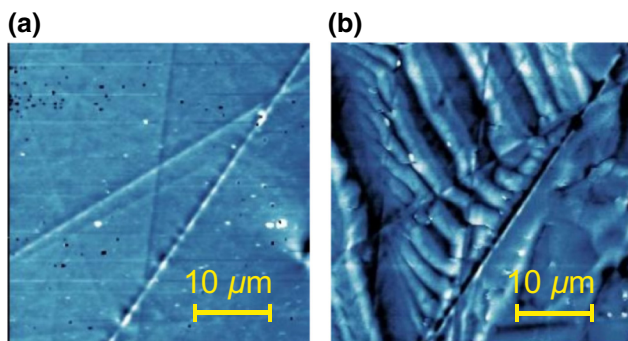


FIG. 4. MFM micrograph of the same area of the YIG/Pt surface at magnetic saturation (a) and at approximately 8 mT (b).

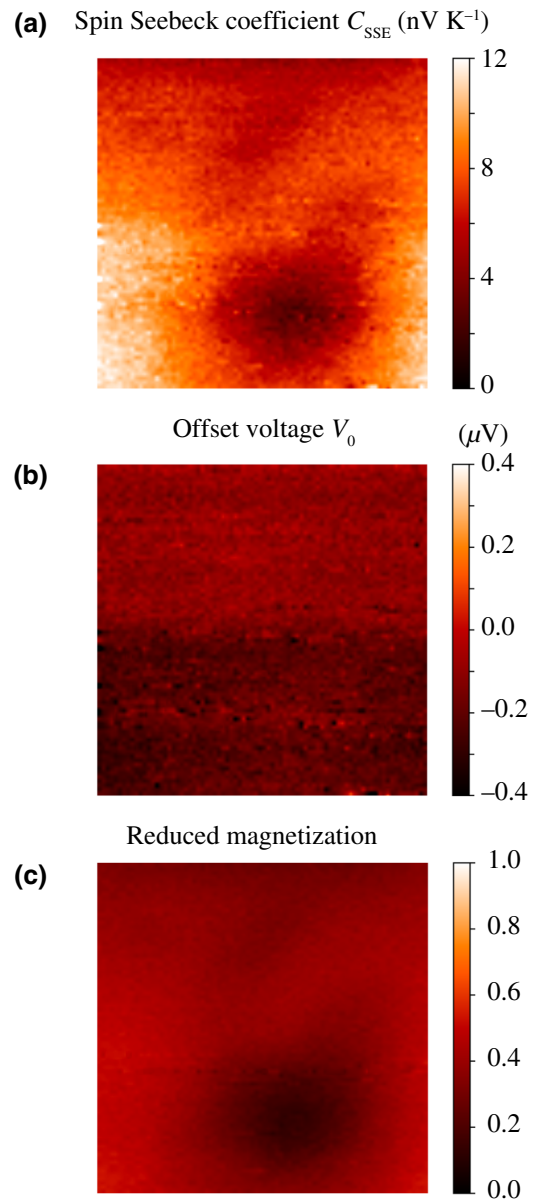


FIG. 5. Spin Seebeck maps of one $80 \times 80 \mu\text{m}^2$ area of the YIG/Pt sample surface obtained with local heating generated by 0.5, 1, 1.5, 1.8, and 2.2 V on the heater. (a) Spin Seebeck coefficients measured at each pixel of the map. (b) Map of the spurious offset-voltage component and (c) map of the ratios between the local spin Seebeck voltage and the corresponding quantity at magnetic saturation; the colour scale in (c) represents the magnetization as a percentage of the magnetic saturation.

investigated. With these data sets we are able to determine the SSE dependence on the heating power and extract the SSE voltage for each pixel of the data set. First we remove the ordinary Seebeck component, as described in Sec. IV B for the sample at magnetic saturation; this procedure gives the spin Seebeck coefficient C_{SSE} and the measurement offset V_0 , represented by the slopes and the intercepts of

the blue lines in Fig. 3. We extract the values of these two parameters for the sample at intermediate magnetization by performing a linear fit of the voltages (V_{meas}) represented by each pixel as a function of the temperature difference. We can now build two maps that represent the parameters of these linear fits: the map of the spin Seebeck coefficients C_{SSE} [Fig. 5(a)] and the map of intercepts V_0 [Fig. 5(b)]. Since we have already measured the upper limit of the spin Seebeck signal (i.e., the value at magnetic saturation), we can use this value to normalize our results with approximately 8 mT, which is represented as a percentage of the maximum signal at saturation. Figure 5(c) shows an example of the result of this procedure recorded at the maximum temperature difference; the color bar quantifies the level of magnetization between zero and the values at saturation, represented as the range from 0 to 1. From the data in Fig. 5(a), we find that the ratio between the spin Seebeck values and the temperature difference (i.e., the spin Seebeck coefficient) has nonzero positive values in some regions and decreases in the central region of the map. By applying the definition of the spin Seebeck coefficient C_{SSE} , where the heat current, voltage, and magnetization (x , y , and z axes, respectively) are orthogonal to each other, as shown in Fig. 1, we can focus on the relationship between C_{SSE} and the magnetization. In the case of uniform heating [Fig. 1(a)] and a sample in the multidomain state, the spin Seebeck voltage depends on the z component of the average magnetization. The dependence of the spin Seebeck voltage on applied magnetic field originates from this relationship, and for the sample used in this study, is reported in the supplementary information in Ref. [34]. For the case of local heat currents, we can now locally probe the z component of the magnetization, whereas in the case of uniform heating, we can probe only its mean value over the entire sample. Therefore, for samples with domain structure, C_{SSE} is a measure of the z component of the local magnetization. In comparison, the map of the intercepts in Fig. 5(b) shows a flatter curve, indicating that the electrical offset is approximately constant over the area investigated.

C. Comparison between MFM and local spin Seebeck images

The third step of this experiment involves scanning different regions of the sample, at a fixed heating voltage, with the same applied magnetic field as previously used (approximately 8 mT). The motivation is a qualitative comparison of the spin Seebeck maps with MFM micrographs. We test the hypothesis that the contrast of the local spin Seebeck map is related to the local magnetization through the local spin Seebeck signal. Scanning of large areas allows the overlapping of neighboring data sets and we record them accordingly; the corresponding MFM micrographs and the local spin Seebeck voltage maps are reported in Fig. 6. The signal of the local spin

Seebeck maps is processed using the data-analysis program GWYDDION [35]. First we focus on the presence of some sharp voltage spikes; these are manually corrected with an interpolation of the error-free pixels surrounding the spike. The second data process concerns the artifacts that usually appear because of the line-by-line acquisition. We correct the voltage shift that arises between neighboring horizontal lines by minimizing the median of the height differences between vertical neighboring pixels [36]. From Fig. 6 we observe that the MFM micrographs can provide a great variety of detail due to the high resolution, whereas the local SSE maps have a lower spatial resolution. Furthermore, we have to keep in mind that the underlying physical phenomena are different for both experiments: the MFM signal depends on the stray fields emanating from the sample surface, whereas the local SSE depends on the magnetization of the sample and the integrated effect over the hot spot provided by the probe. Moreover, it is speculated that the local SSE signal originates from a volume of the sample that is defined by the top surface and by the magnon diffusion length in YIG within the sample. For this reason, any qualitative difference found between the MFM features and the local SSE features can be attributed to the contribution of deeper layers within the sample to the SSE signal not observed in the interaction volume experienced by the MFM probe. However, at this stage we focus on the correspondence between features in the MFM micrographs and regions of local minima of the local spin Seebeck maps. To make the correlation more visible, we trace the contour lines extracted by the spin Seebeck maps above the MFM micrographs in Fig. 6. For the three images on the left, we select the contour lines corresponding to $0.6 \mu\text{V}$ in the spin Seebeck map, while for the two images on the right we select different values since we do observe a drift in the offset voltage. For this reason, the two areas labeled by the green and light-blue frames appear on a slightly different voltage scale, but nevertheless it is possible to distinguish the shape of the local minimum in the expected position, according to the $20\text{-}\mu\text{m}$ shift between the two areas. The two micrographs that refer to the area labeled by the red frame in Fig. 6 represent a measurement across the edge of the Pt strip, cutting the frame horizontally. In the lower half of the SSE micrograph (the region not covered by the Pt), the spin Seebeck voltage decreases in agreement with the local generation of a spin current from the bare YIG that is not detected by the Pt film. Finally, it is possible to use the local spin Seebeck maps to measure the magnetization of the sample. By assuming a constant permeability, we can refer to the spin Seebeck voltage as a function of the magnetic field applied to the sample according to the hysteresis loop (see the supplementary information in Ref. [34]). The upper limit for the local spin Seebeck voltage is expressed by its average value at saturation and is associated with the saturating field for this sample (approximately 20 mT).

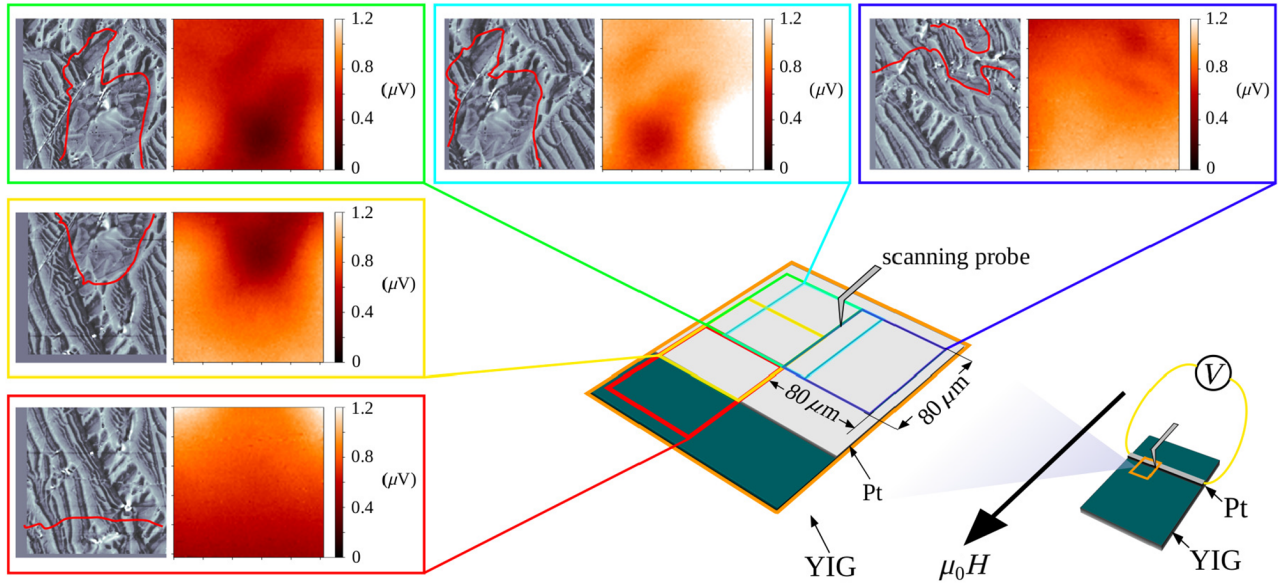


FIG. 6. Local spin Seebeck voltage maps (right columns) obtained at approximately 8 mT with 1.5 V at the heater, shown together with the MFM micrographs (left columns). The five pairs of maps correspond to the areas of the sample represented in the scheme, where the edge of the Pt film is shown, together with the direction of the applied magnetic field.

The ratio between the average local spin Seebeck voltages for the sample in the multidomain state (i.e., the average of all values shown in the maps in Fig. 6) and the limits at saturation corresponds to a value of 0.4. This ratio multiplied by the saturation field is consistent with the values of the measurement performed with the Hall probe (8 mT) at field strengths below the saturation field. With reference to the sample SSE hysteresis loop mentioned above, an applied magnetic field of 8 mT sets the magnetization above the level where the magnetic field dependence of the SSE deviates from the bulk magnetization curve [37,38]. This has also been reported for experiments performed on other bulk samples [19,20,23,39–41].

D. Spatial resolution of the spin Seebeck image

Finally, we comment on the resolution of the local SSE measurement technique. We consider the radius of the hot spot [r_0 in Eq. (2)] as a more-realistic limit to the resolution compared with the cross section of the probe. Starting from the thermodynamic description of the SSE, we derive the expression for the spin Seebeck voltage difference as a function of the heat current injected by the heated AFM probe. We also highlight the need to rescale this expression according to the geometry of the experiment, as represented by Eq. 3. By replacing the expression for the spin Seebeck voltage ΔV_{SSE} [Eq. (2)] in the expression for the rescaled signal, we derive the following representation of the experimental results:

$$\frac{\Delta V_{\text{SSE,exp}}}{\Delta T} = \frac{4r_0}{L_z} \theta_{\text{SH}} \left(\frac{\mu_B}{e} \right) \frac{v_{\text{YIG}} I_{\text{YIG}} \epsilon_{\text{YIG}}}{v_p} \frac{1}{t_{\text{Pt}}}, \quad (5)$$

where the parameters that represent the properties of YIG are chosen according to the semi-infinite approximation, where the thickness of the YIG is greater than the magnon diffusion length, and $L_z = 150 \mu\text{m}$ is the width of the Pt strip. In Eq. (5) the heat current I_q that appears in Eq. (2) is written as the temperature difference ΔT , by our knowing the thermal conductivity κ and the geometrical constraints on the YIG layer. By using the experimental data from a previous spin Seebeck study on the same sample [34], we can use the following experimental value for the YIG:

$$\frac{v_{\text{YIG}} I_{\text{YIG}} \epsilon_{\text{YIG}}}{v_p} = -4.6 \times 10^{-10} \text{ V K}^{-1} \text{ m}^{-1} \text{ s}. \quad (6)$$

The spin Hall angle $\theta_{\text{SH}} = -0.1$ refers to the current of magnetic moments that has the opposite sign with respect to a definition of the spin Hall angle based on the spin current [34]. By using the value of the spin Seebeck coefficient obtained ($C_{\text{SSE}} = 2 \times 10^{-8} \text{ V K}^{-1}$) in place of $\Delta V_{\text{SSE,exp}}/\Delta T$ in Eq. (5), we obtain $r_0 = 1.4 \mu\text{m}$. This value of r_0 is in reasonable agreement with the lateral point-spread function of a heating laser presented by Bartell *et al.* [28] with a FWHM of the hot spot of $0.606 \mu\text{m}$ obtained with an optical laser power of 0.6 mW.

V. CONCLUSIONS

In summary, we use a scanning-probe-microscopy technique to locally inject heat currents in a YIG/Pt bilayer structure. We observed a spatially resolved voltage response dependent on the location of the heated

probe and the local magnetization state that we unambiguously attribute to the SSE. This allows us to obtain locally resolved spin Seebeck measurements, which we map spatially and compare qualitatively with MFM micrographs obtained on the same scanned regions. We discuss the measured signals using a thermodynamic description in spherical coordinates. Furthermore, we derive the spatial resolution of the local spin Seebeck measurements, which is on the order of few micrometers. Local spin Seebeck imaging is an innovative tool for the investigation of spin-caloritronic materials. In particular, it provides a significant step forward for the analysis of bulk magnetic structures compared with surface characterization techniques, as the signal originates from the bulk at a distance that can be considered equivalent to the magnon diffusion length. Additionally, this experimental technique allows us to image the magnetization structure of samples where tip-sample interaction could result in irreversible changes of the sample state during the imaging process, thus providing a nonperturbative imaging tool. Moreover, this technique could pave the way to alternative concepts of scanning-probe microscopy inspired by spintronics and spin caloritronics; for example, the development of V-shaped Pt probes as a point-contact inverse-spin-Hall-effect detector, or scanning thermal microscopy as a probe for spatial magnetic imaging using the spin Peltier effect.

ACKNOWLEDGMENTS

The authors thank the European Metrology Research Programme (EMRP) Joint Research Project 15SIB06 NanoMag for financial support. In particular, A.S. acknowledges Researcher Mobility Grant No. 15SIB06-RMG3. The EMRP is jointly funded by the EMRP participating countries within EURAMET and the European Union. The authors thank Dr. Vladimir Antonov, Royal Holloway, University of London, for Pt deposition. A.S. thanks Marco Coisson for useful discussions and preliminary MFM measurements. C.D. thanks R. Meyer and B. Wenzel for technical assistance.

-
- [1] Y. Martin and H. Kumar Wickramasinghe, Magnetic imaging by force microscopy with 1000 Å resolution, *Appl. Phys. Lett.* **50**, 1455 (1987).
- [2] J. J. Saenz, N. Garcia, P. Grütter, E. Meyer, H. Heinzelmann, R. Wiesendanger, L. Rosenthaler, H. R. Hidber, and H. J. Güntherodt, Observation of magnetic forces by the atomic force microscope, *J. Appl. Phys.* **62**, 4293 (1987).
- [3] M. R. Scheinfein, J. Unguris, M. H. Kelley, D. T. Pierce, and R. J. Celotta, Scanning electron microscopy with polarization analysis (SEMPA), *Rev. Sci. Instrum.* **61**, 2501 (1990).
- [4] A. Hubert and R. Schäfer, *Magnetic Domains: the Analysis of Magnetic Microstructures* (Springer Science & Business Media, Berlin, 2008).
- [5] J. N. Chapman and M. R. Scheinfein, Transmission electron microscopies of magnetic microstructures, *J. Magn. Magn. Mater.* **200**, 729 (1999).
- [6] A. Tonomura, Applications of electron holography, *Rev. Mod. Phys.* **59**, 639 (1987).
- [7] O. Halpern and T. Holstein, On the passage of neutrons through ferromagnets, *Phys. Rev.* **59**, 960 (1941).
- [8] F. Pfeiffer, C. Grünzweig, O. Bunk, G. Frei, E. Lehmann, and C. David, Neutron Phase Imaging and Tomography, *Phys. Rev. Lett.* **96**, 215505 (2006).
- [9] C. Grünzweig, C. David, O. Bunk, M. Dierolf, G. Frei, G. Kühne, J. Kohlbrecher, R. Schäfer, P. Lejcek, H. M. R. Rønnow, *et al.*, Neutron Decoherence Imaging for Visualizing Bulk Magnetic Domain Structures, *Phys. Rev. Lett.* **101**, 025504 (2008).
- [10] A. Hilger, I. Manke, N. Kardjilov, M. Osenberg, H. Markötter, and J. Banhart, Tensorial neutron tomography of three-dimensional magnetic vector fields in bulk materials, *Nat. Commun.* **9**, 4023 (2018).
- [11] R. Streubel, F. Kronast, P. Fischer, D. Parkinson, O. G. Schmidt, and D. Makarov, Retrieving spin textures on curved magnetic thin films with full-field soft x-ray microscopies, *Nat. Commun.* **6**, 7612 (2015).
- [12] C. Donnelly, M. Guizar-Sicairos, V. Scagnoli, M. Holler, T. Huthwelker, A. Menzel, I. Vartiainen, E. Müller, E. Kirk, S. Gliga, *et al.*, Element-Specific X-ray Phase Tomography of 3D Structures at the Nanoscale, *Phys. Rev. Lett.* **114**, 115501 (2015).
- [13] M. Dierolf, A. Menzel, P. Thibault, P. Schneider, C. M. Kewish, R. Wepf, O. Bunk, and F. Pfeiffer, Ptychographic x-ray computed tomography at the nanoscale, *Nature* **467**, 436 (2010).
- [14] K. Uchida, S. Takahashi, K. Harii, J. Ieda, W. Koshibae, K. Ando, S. Maekawa, and E. Saitoh, Observation of the spin Seebeck effect, *Nature* **455**, 778 (2008).
- [15] A. Kehlberger, U. Ritzmann, D. Hinzke, E. J. Guo, J. Cramer, G. Jakob, M. C. Onbasli, D. H. Kim, C. A. Ross, M. B. Jungfleisch, *et al.*, Length Scale of the Spin Seebeck Effect, *Phys. Rev. Lett.* **115**, 096602 (2015).
- [16] E. J. Guo, J. Cramer, A. Kehlberger, C. A. Ferguson, D. A. MacLaren, G. Jakob, and M. Kläui, Influence of Thickness and Interface on the Low-Temperature Enhancement of the Spin Seebeck Effect in YIG Films, *Phys. Rev. X* **6**, 031012 (2016).
- [17] V. Basso, P. Ansalone, and M. Piazza, Non-equilibrium thermodynamic approach to spin pumping and spin Hall torque effects, *J. Phys. D: Appl. Phys.* **51**, 214006 (2018).
- [18] K. Uchida, J. Xiao, H. Adachi, J. Ohe, S. Takahashi, J. Ieda, T. Ota, Y. Kajiwara, H. Umezawa, H. Kawai, G. E. W. Bauer, S. Maekawa, and E. Saitoh, Spin Seebeck insulator, *Nat. Mater.* **9**, 894 (2010).
- [19] K. Uchida, T. Nonaka, T. Ota, and E. Saitoh, Longitudinal spin-Seebeck effect in sintered polycrystalline (Mn, Zn) Fe₂O₄, *Appl. Phys. Lett.* **97**, 262504 (2010).
- [20] K. Uchida, T. Nonaka, T. Kikkawa, Y. Kajiwara, and E. Saitoh, Longitudinal spin Seebeck effect in various garnet ferrites, *Phys. Rev. B* **87**, 104412 (2013).
- [21] D. Meier, T. Kuschel, L. Shen, A. Gupta, T. Kikkawa, K. Uchida, E. Saitoh, J. M. Schmalhorst, and G. Reiss, Thermally driven spin and charge currents in thin NiFe₂O₄/Pt films, *Phys. Rev. B* **87**, 054421 (2013).

- [22] E. Saitoh, M. Ueda, H. Miyajima, and G. Tatara, Conversion of spin current into charge current at room temperature: Inverse spin-Hall effect, *Appl. Phys. Lett.* **88**, 182509 (2006).
- [23] K. Uchida, H. Adachi, T. Ota, H. Nakayama, S. Maekawa, and E. Saitoh, Observation of longitudinal spin-Seebeck effect in magnetic insulators, *Appl. Phys. Lett.* **97**, 172505 (2010).
- [24] K. Uchida, M. Ishida, T. Kikkawa, A. Kirihara, T. Murakami, and E. Saitoh, Longitudinal spin Seebeck effect: From fundamentals to applications, *J. Phys.: Condens. Matter* **26**, 343202 (2014).
- [25] D. Meier, D. Reinhardt, M. van Straaten, C. Klewe, M. Althammer, M. Schreier, S. T. B. Goennenwein, A. Gupta, M. Schmid, C. H. Back, *et al.*, Longitudinal spin Seebeck effect contribution in transverse spin Seebeck effect experiments in Pt/YIG and Pt/NFO, *Nat. Commun.* **6**, 8211 (2015).
- [26] M. Weiler, M. Althammer, F. D. Czeschka, H. Huebl, M. S. Wagner, M. Opel, I. M. Imort, G. Reiss, A. Thomas, R. Gross, *et al.*, Local Charge and Spin Currents in Magnetothermal Landscapes, *Phys. Rev. Lett.* **108**, 106602 (2012).
- [27] N. Roschewsky, M. Schreier, A. Kamra, F. Schade, K. Ganzhorn, S. Meyer, H. Huebl, S. Geprägs, R. Gross, and S. T. B. Goennenwein, Time resolved spin Seebeck effect experiments, *Appl. Phys. Lett.* **104**, 202410 (2014).
- [28] J. M. Bartell, C. L. Jermain, S. V. Aradhya, J. T. Brangham, F. Yang, D. C. Ralph, and G. D. Fuchs, Imaging Magnetization Structure and Dynamics in Ultrathin $\text{Y}_3\text{Fe}_5\text{O}_{12}$ /Pt Bilayers with High Sensitivity Using the Time-Resolved Longitudinal Spin Seebeck Effect, *Phys. Rev. Appl.* **7**, 044004 (2017).
- [29] J. S. Jamison, Z. Yang, B. L. Giles, J. T. Brangham, G. Wu, P. C. Hammel, F. Yang, and R. C. Myers, Long lifetime of thermally excited magnons in bulk yttrium iron garnet, *Phys. Rev. B* **100**, 134402 (2019).
- [30] J. M. Bartell, D. H. Ngai, Z. Leng, and G. D. Fuchs, Towards a table-top microscope for nanoscale magnetic imaging using picosecond thermal gradients, *Nat. Commun.* **6**, 8460 (2015).
- [31] V. Basso, M. Kuepferling, A. Sola, P. Ansalone, and M. Pasquale, The spin Seebeck and spin peltier reciprocal relation, *IEEE Magnetics Lett.* **9**, 1 (2018).
- [32] V. Castel, N. Vlietstra, J. B. Youssef, and B. J. van Wees, Platinum thickness dependence of the inverse spin-Hall voltage from spin pumping in a hybrid yttrium iron garnet/platinum system, *Appl. Phys. Lett.* **101**, 132414 (2012).
- [33] H. L. Wang, C. H. Du, Y. Pu, R. Adur, P. C. Hammel, and F. Y. Yang, Scaling of Spin Hall Angle in 3d, 4d, and 5d Metals from $\text{Y}_3\text{Fe}_5\text{O}_{12}$ /metal Spin Pumping, *Phys. Rev. Lett.* **112**, 197201 (2014).
- [34] A. Sola, V. Basso, M. Kuepferling, C. Dubs, and M. Pasquale, Experimental proof of the reciprocal relation between spin Peltier and spin Seebeck effects in a bulk YIG/Pt bilayer, *Sci. Rep.* **9**, 2047 (2019).
- [35] D. Nečas and P. Klapetek, Gwyddion: An open-source software for SPM data analysis, *Open Phys.* **10**, 181 (2012).
- [36] P. Klapetek, *Quantitative Data Processing in Scanning Probe Microscopy: SPM Applications for Nanometrology* (Elsevier, Amsterdam, 2018).
- [37] K. Uchida, J. Ohe, T. Kikkawa, S. Daimon, D. Hou, Z. Qiu, and E. Saitoh, Intrinsic surface magnetic anisotropy in $\text{Y}_3\text{Fe}_5\text{O}_{12}$ as the origin of low-magnetic-field behavior of the spin Seebeck effect, *Phys. Rev. B* **92**, 014415 (2015).
- [38] V. Kalappattil, R. Das, M. H. Phan, and H. Srikanth, Roles of bulk and surface magnetic anisotropy on the longitudinal spin Seebeck effect of Pt/YIG, *Sci. Rep.* **7**, 13316 (2017).
- [39] T. Kikkawa, K. Uchida, Y. Shiomi, Z. Qiu, D. Hou, D. Tian, H. Nakayama, X. F. Jin, and E. Saitoh, Longitudinal Spin Seebeck Effect Free from the Proximity Nernst Effect, *Phys. Rev. Lett.* **110**, 067207 (2013).
- [40] T. Kikkawa, K. Uchida, S. Daimon, Y. Shiomi, H. Adachi, Z. Qiu, D. Hou, X. F. Jin, S. Maekawa, and E. Saitoh, Separation of longitudinal spin Seebeck effect from anomalous Nernst effect: Determination of origin of transverse thermoelectric voltage in metal/insulator junctions, *Phys. Rev. B* **88**, 214403 (2013).
- [41] T. Kikkawa, K. Uchida, S. Daimon, Z. Qiu, Y. Shiomi, and E. Saitoh, Critical suppression of spin Seebeck effect by magnetic fields, *Phys. Rev. B* **92**, 064413 (2015).